The many faces of radiation-induced changes

Dominika Borek,[a] Stephan L. Ginell,[b] Marcin Cymborowski,[c] Wladek Minor[c] and Zbyszek Otwinowski[a]*

[a]Department of Biochemistry, University of Texas, Southwestern Medical Center at Dallas, 5323 Harry Hines Boulevard, Dallas, TX 75390, USA, [b]Structural Biology Center, Argonne National Laboratory, 9700 South Cass Avenue, Argonne, IL 60439, USA, and [c]Department of Molecular Physiology and Biological Physics, University of Virginia, Jordan Hall, 1300 Jefferson Park Avenue, Charlottesville, VA 22908, USA. E-mail: zbyszek@work.swmed.edu

During diffraction experiments even cryo-cooled protein crystals can be significantly damaged due to chemical and physical changes induced by absorbed X-ray photons. The character and scale of the observed effects depend strongly on the temperature and the composition of crystals. The absorption of radiation energy results in incremental regular changes to the crystal structure, making its impact on the process of solving the structure strongly correlated with other experimental variables. An understanding of all the dependencies is still limited and does not allow for a precise prediction of the outcome of a particular diffraction experiment. Results are presented of diffraction experiments performed under different experimental conditions. The influence of temperature and crystal composition on different characteristics of radiation damage is analyzed. The observed effects are discussed in terms of their impact on data processing and phasing procedures.

1. Introduction

Intense X-ray sources combined with cryo-cooling devices allow for structural studies of small and/or poorly ordered macromolecular crystals. However, even cryo-cooled crystals undergo changes resulting from reactions induced by the absorption of X-ray photons (Teng & Moffat, 2000; Weik *et al.*, 2000; Ravelli & McSweeney, 2000; Burmeister, 2000). In recent years crystallographers have come to see radiation damage as the main source of systematic effects which can easily corrupt the phasing signal. Traditional procedures correct for the overall decay resulting from radiation damage; however, the specific changes are more complex and need more elaborate calculations to correct for them, or even use them as a source of phasing signal. The first steps in this direction show promising results, but have not yet become widely used (Ramagopal *et al.*, 2005; Diederichs, 2006; Diederichs *et al.*, 2003; Ravelli *et al.*, 2003). There are two reasons for this: (i) the character of the changes varies, so the models and procedures need to be more sophisticated; (ii) the computational programs need to be easy to use, efficient and stable. In this article we describe the magnitude and the type of various effects in X-ray exposed crystals of macromolecules. This information is equally important for designing diffraction experiments and in developing new software to correct and/or use radiation-induced changes (Otwinowski *et al.*, 2007).

There are five categories of the observed effects: resolution-independent decay, overall resolution-dependent decay, localized structural changes, unit-cell changes and macroscopic crystal-order changes. The cascade of physical events starts with photoelectrons resulting from X-ray absorption. These photoelectrons have starting energies close to that of the incoming X-rays and, travelling in the crystal, produce the majority of radiation damage while losing energy. The range of these electrons' penetration is of the order of a micrometre, so virtually all of them are stopped in the crystal (Owen *et al.*, 2006; Nave, 1995; Nave & Hill, 2005). On the other hand, the distance travelled is much larger than the size of molecules and crystal unit cells, so the site of radiation damage is essentially uncorrelated with the atomic position where the absorption occurs. The increase in the changes localized at the point of absorption is attenuated by the high number of free radicals produced from the absorption of a single photon. What matters most to radiation damage is the total energy absorbed per unit volume, and not how it can be produced by different combinations of X-ray energy, absorption coefficient and flux. The slowdown of photoelectrons results in the production of free radicals that subsequently migrate and interact with molecules in the solvent and the protein. There are many possible chemical interactions, whose detailed chemistry is now being elucidated (Weik *et al.*, 2002; O'Neill *et al.*, 2002; Burmeister, 2000). One would naively expect that,

since all the proteins are built from the same amino acids with similar structural motifs, the structural changes will be quite uniform among proteins. To some extent this has been confirmed by many observations, including some of those presented here, that disulphide bridges and carboxyl groups tend to be the most sensitive to radiation damage. There are crystal structures where such localized atomic displacements are the dominant source of structure factor changes induced by radiation damage. This led to the idea of a radiation-induced phasing method (Ravelli *et al.*, 2003), but the question arises as to how often and/or in what type of projects favourable conditions appear, and what to do if they are not so. So far, this problem has not been analysed for a larger range of crystals. To address that need, we present an analysis of radiation damage in different types of crystals with diverse heavy-atom content and of a case with a free-radical scavenger. Additionally we show how the different characteristics of radiation damage change with temperature over the 15–200 K range.

2. Experimental procedures

2.1. Crystallization

All proteins were crystallized by the vapour diffusion method in hanging drops. Glucose isomerase (GI) from *Streptomyces rubiginosus* was purchased from Hampton Research. The protein was dialyzed three times against water and concentrated. GI-Ca crystals with 0.25 mm × 0.25 mm × 0.2 mm dimensions grew in 1–2 weeks from drops containing 25 mg ml^{-1} of protein diluted at a 1:1 ratio (v/v) with a reservoir solution comprising 0.1 M CaCl$_2$, 16–22% MPD and 0.1 M Tris-HCl pH 7.0. GI-Mg crystals with 0.15 mm × 0.15 mm × 0.2 mm dimensions grew in 1–2 weeks from drops containing 25 mg ml^{-1} of protein diluted at a 1:1 ratio (v/v) with reservoir solution comprising 0.15 M MgCl$_2$, 20% MPD and 0.1 M Tris-HCl pH 7.0. Both GI-Ca and GI-Mg crystals were flash-cooled in liquid propane directly from crystallization drops. As expected, in both cases $F_o - F_c$ and anomalous difference maps identified manganese ions bound to the protein, either carried over from the protein purification or contributed by salt impurity.

Thaumatin (TH) from *Thaumatococcus danielli* was purchased from Sigma-Aldrich (St Louis, MO, USA; Cat. No. T7638). The protein was dissolved in water to a concentration of 50 mg ml^{-1} and filtered through a 0.2 µm filter by centrifugation. Crystals with 0.25 mm × 0.25 mm × 0.4 mm dimensions grew in 2–4 days from drops containing 25 mg ml^{-1} of protein diluted at a 1:1 ratio (v/v) with a reservoir solution comprising 1.0 M potassium, sodium tartrate, 15% ethylene glycol and 0.1 M Hepes-Na pH 6.75. The crystals were flash-cooled in liquid propane directly from crystallization drops.

Catalase (CAT) from bovine liver was purchased from Sigma-Aldrich (Cat. No. C100). The protein was filtered through a 0.2 µm filter by centrifugation and used for crystallization without further dilution or concentration. Crystals with 0.2 mm × 0.25 mm × 0.35 mm dimensions grew from drops containing 25 mg ml^{-1} of protein diluted at 1:1 ratio (v/v) with a reservoir solution comprising 8–12% polyethylene glycol 8000, 22–26% polyethylene glycol 400 and 0.1 M Tris-HCl pH 8.3. Catalase crystals were flash-cooled in liquid propane directly from crystallization drops.

Lysozyme (L) from chicken egg white was purchased from Sigma-Aldrich (Cat. No. L6876). 100 mg of the protein was dissolved in 1 ml of distilled water and dialyzed overnight against water. Monoclinic-form crystals (LM) with 0.1 mm × 0.1 mm × 0.3 mm dimensions grew from drops containing 100 mg ml^{-1} of protein diluted at a 1:1 ratio (v/v) with the reservoir solution comprising 2% sodium nitrate and 0.05 M sodium acetate pH 4.6. Monoclinic-form lysozyme crystals were flash-cooled in liquid propane after a short soak in the reservoir solution augmented with glycerol to 30% concentration. Tetragonal-form lysozyme crystals (LT) with 0.25 mm × 0.25 mm × 0.25 mm dimensions grew from drops containing 100 mg ml^{-1} of protein diluted at a 1:1 ratio (v/v) with the reservoir solution comprising 0.5 M sodium chloride and 0.05 M sodium acetate pH 4.5. Tetragonal-form lysozyme crystals were flash-cooled in liquid propane after a short soak in the reservoir solution augmented with ethylene glycol to 30% concentration.

MCSG target APC35841 (NaI-841) was crystallized at 293 K. The protein concentrated to 11 mg ml^{-1} was diluted at a 1:1 ratio (v/v) with a well solution of 0.1 M Tris-HCl pH 8.0 and 1.68 M ammonium sulfate. Crystals with 0.35 mm × 0.35 mm × 0.4 mm dimensions appeared after 14 days. Before flash-cooling they were soaked for 30–60 s in the well solution supplemented to achieve 0.5 M sodium iodide and 25% ethylene glycol concentrations.

Crystallization conditions for a mutant of bovine pancreatic trypsin inhibitor [BPTI; Protein Data Bank (PDB) code: 1G6X] and cobalamin transporter BtuB (PDB code: 1NQF) are described in articles presenting structure solutions (Chimento *et al.*, 2003; Addlagatta *et al.*, 2001).

Crystallization conditions for crystals used to test synchrotron beamline conditions were modified from the 15 min lysozyme recipe by Stura (1998). 100 mg ml^{-1} Lysozyme in 0.05 M sodium acetate buffered to pH 4.6 was mixed at a 1:1 ratio with a well solution containing 30% (w/v) of MPEG 5000 (polyethylene glycol 5000 monomethyl ether), 0.05 M sodium acetate buffered to pH 4.6, 0.3 M sodium iodide and 5% (v/v) of ethylene glycol so the crystals could easily be cryo-cooled using either liquid nitrogen or propane.

2.2. Data collection and processing

Except for the BPTI (Addlagatta *et al.*, 2001) crystals, all other data were collected at beamline 19BM or 19ID of the Structural Biology Center situated at the Advance Photon Source, Argonne National Laboratory. Most data were collected with crystals cryo-cooled by a nitrogen stream with a temperature in the range 105–112 K. The three data sets from separate GI-Ca crystals cooled to 15, 40 and 80 K were collected using an open flow helium cryostat (CRYO Indus-

radiation damage

Table 1
Data collection and processing statistics for GI-Ca data collected at different temperatures.

The data processing statistics are for all collected data sets for each crystal scaled together.

	GI-Ca-15	GI-Ca-40	GI-Ca-80	GI-Ca-130	GI-Ca-140	GI-Ca-160	GI-Ca-200
Temperature (K)	15	40	80	130	140	160	200
Wavelength (Å)	0.9792	0.9792	0.9792	0.9792	0.9792	0.9792	0.9792
Oscillation range per run (°)	240	240	240	240	240	240	240
Oscillation step (°)	1	1	1	1	1	1	1
Exposure time per data set (s)	240	240	480	480	480	480	480
Number of data sets used	6	8	4	4	4	4	2
Space group	$I222$	$I222$	$I222$	$I222$	$I222$	$I222$	$I222$
Unit cell (Å)	$a = 92.85$	$a = 92.85$	$a = 92.86$	$a = 93.05$	$a = 93.00$	$a = 93.14$	$a = 93.49$
	$b = 98.04$	$b = 98.05$	$b = 97.78$	$b = 98.30$	$b = 98.26$	$b = 98.19$	$b = 97.72$
	$c = 102.26$	$c = 102.32$	$c = 102.41$	$c = 102.50$	$c = 102.55$	$c = 102.59$	$c = 102.77$
Resolution	50.0–1.7	50.0–1.7	50.0–1.7	50.0–1.7	50.0–1.7	50.0–1.7	50.0–1.7
No. of unique reflections	51709	49592	51580	51081	51644	51578	51744
No. of unique reflections used for radiation damage analysis	49156	46514	50472	49805	50730	48824	48824
$\langle I/\sigma_I\rangle$/last shell	129.7/53.9	154.1/108.7	131.4/67.3	190.4/102.6	110.6/42.8	154.6/86.8	81.6/38.9

tries of America), and four data sets at 130, 140, 160 and 200 K were collected using a nitrogen cryostat. Temperatures were recorded from a cryo-controller. During this temperature series the intensity of the beam was approximately constant. For data collected at 15 K, we observed an accumulation of frozen air, which with time changed the quality of the diffraction images. For this reason we removed from the analysis the last two data sets (out of eight) for that temperature. At each temperature a series of identical oscillation ranges was collected and the radiation damage rates were estimated by a global fit and/or by calculating differences between scaled individual oscillation ranges. All data were indexed, integrated and scaled using the *HKL2000* suite of programs (Otwinowski & Minor, 1997, 2000). The scaled observed intensities were fitted by a separate least-squares procedure for every unique *hkl* reflection. The unknown parameters in general were the diffraction intensity at zero dose, the linear change of intensity with the dose, and the Bijvoet's difference. If the estimated error of slope coefficients or Bijvoet's difference were significantly larger than their expected value based on the resolution, the least-squares procedure was repeated with these coefficients being omitted. A description of the data collection and processing is presented in Tables 1 and 2.

2.3. Radiation damage assessment and the choice of its indicators

Owing to experimental limitations in the focusing optics, the X-ray beam was not uniform, and frequently crystals were somewhat larger than the beam size. For this and other reasons, when the data were collected over a long period of time, we are not in a position to be certain about the absolute calibration of the X-ray dose. It has been observed (Owen *et al.*, 2006) that the increase in scaling *B*-factor is strongly correlated with the dose; also, the proportionality constant varied little in the group of samples tested at the same temperature (Kmetko *et al.*, 2006). From the point of view of a physicist or a chemist, the dose is the preferred reference for

the description of radiation damage. However, a crystallographer solving a structure will typically be able to estimate the increase in scaling *B*-factor much more reliably than they are able to calculate the dose from the beamline intensity monitor and a knowledge of the relevant geometrical factors (beamline profile, crystal shape, size and its exact relation to the rotation axis). Since structure factor changes are approximately a linear function of the dose (Banumathi *et al.*, 2004), even when the crystal is not uniformly exposed, the consequences of the radiation damage are the same as if the crystal were uniformly exposed to the average dose.

For these reasons we use the increase in *B*-factor as a reference to estimate the extent of radiation damage. However, the scaling *B*-factor correlation with dose is dependent on temperature. For the temperature series, we designed the experiments in such a way that a group of similar-size crystals was exposed to a beam of constant intensity over the same periods of time. This allowed us to establish how the decay rate (increase in scaling *B*-factor to dose ratio) depends on the crystal temperature.

If we are analysing the real-space pattern of radiation damage, then, in a linear approximation, the non-uniformity of exposure or even a lack of absolute calibration does not affect the result. All the results presented were calculated with a linear interpolation of structure factor changes corrected for the *B*-factor increase, thus the Fourier transform of the slope coefficients reveals the spatial distribution of the initial rate of change. This map, calculated with the refined model phases, can be equally well considered as a difference map between the zero dose and any accumulated dose where the assumption of linearity is still valid. Peak heights are in σ, root-mean-square units of the map.

We also calculate the average magnitude of the structure factor changes relative to the native structure factors, $R_R = \langle \Delta F^2 \rangle^{1/2}/\langle F^2 \rangle^{1/2}$. The use of R_R, the magnitude of specific structural changes, should take into account its weak resolution dependence, and the fact that it is not easy to estimate if relative experimental errors are larger than R_R. These issues need to be addressed in detail separately; however, they do

Table 2
Data collection and processing statistics for data sets collected at 105–112 K.

Data processing statistics are for all collected data sets for each crystal scaled together.

	1G6X	1NQF	CAT	GI-Mg	LT	LM	TH	NaI-841
Beamline	X11	19ID	19ID	19BM	19BM	19BM	19BM	19BM
Wavelength (Å)	0.9090	0.9794	0.9792	2.0664	1.6083	0.979	1.9074	1.7280
Oscillation range per data set (°)	90	240	90 (run 1, 2, 3)	240	110	230	120.8	180
Oscillation step (°)	0.5 (run 1) 1.0 (run 2) 2.0 run 3 3.0 (run 4)	1.0 (all runs)	1.0 (all runs)	2 (all runs)	0.5 (all runs)	0.5 (all runs)	0.4	0.6
Exposure time per data set (s)	N/A	240	90 (run 1, 2) 450 (run 3)	1200 (run 1) 3600 (run 2, 3)	110	1610	6040	180
Number of data sets	4	1	3	3	3	3	2	1
Space group	$P4_32_12$	$P3_121$	$P2_12_12_1$	$I222$	$P4_32_12$	$P2_1$	$P4_22_12$	$P4_12_12$
Unit cell (Å; °)	$a = b = 51.89$ $c = 43.03$ $\alpha = \beta = \gamma = 90$	$a = b = 81.61$ $c = 226.65$ $\alpha = \beta = 90$ $\gamma = 120.00$	$a = 83.52$ $b = 140.40$ $c = 229.80$ $\alpha = \beta = \gamma = 90$	$a = 92.91$ $b = 98.7$ $c = 102.59$ $\alpha = \beta = \gamma = 90$	$a = b = 78.88$ $c = 36.89$ $\alpha = \beta = \gamma = 90$	$a = b = 51.89$ $c = 43.03$ $\alpha = \gamma = 90$ $\beta = 90.282$	$a = b = 57.63$ $c = 150.03$ $\alpha = \beta = \gamma = 90$	$a = b = 118.1$ $c = 124.11$ $\alpha = \beta = \gamma = 90$
Resolution	20.00–0.87	50.00–2.68	50.00–1.9	50.00–2.6	50.00–2.0	50.00–2.0	50.00–2.4	50.00–2.95
No. of unique reflections	46275	24581	213255	13820	7829	11746	10572	18993
No. of unique reflections used for anomalous signal analysis	27642	10189	48347	11973	5495	10444	8147	8766
No. of unique reflections used for radiation damage analysis	35530	16667	133906	13534	6642	10877	10307	11081
R_{merge} (after correction for radiation damage)	0.024	0.069	0.081	0.029	0.022	0.053	0.033	0.095
$\langle I/\sigma_I\rangle$/last shell	117.3/5.0	38.8/2.1	31.5/6.0	129.3/72.0	125.6/23.9	55.9/24.7	126.5/58.7	23.5/1.9
Overall redundancy	8.7	12.2	10.6	24.3	19.5	13.1	21.9	8.5

not affect the descriptive nature of R_R for the structure factor changes when we calculate R_R in the resolution shell around 4 Å, where the measurement data quality is very high. We also present the ratio of R_R to B-factor increase as the estimate of the relative magnitude of structure change to diffraction decay.

3. Results and discussion

3.1. Characteristics of radiation damage

3.1.1. Temperature dependence. The measurements of separate GI-Ca crystals were carried out at temperatures that varied from 15 K to 200 K. Most of the radiation damage characteristics show a strong dependence on temperature. The characteristics most important for data quality, ΔB/(exposure time) and R_R/(exposure time), increase monotonically across the whole range of temperatures, with the steepest increase above 140 K (Fig. 1, Table 3), and for 200 K the B-factor increases dramatically. In order to present all the temperature data together, a logarithmic scale had to be used in the graphics, but when interpreting the plot it should be remembered that the B-factor contributes to the diffraction intensities through an exponential term, so that the diffraction intensity is the exponent-of-exponent function of the position
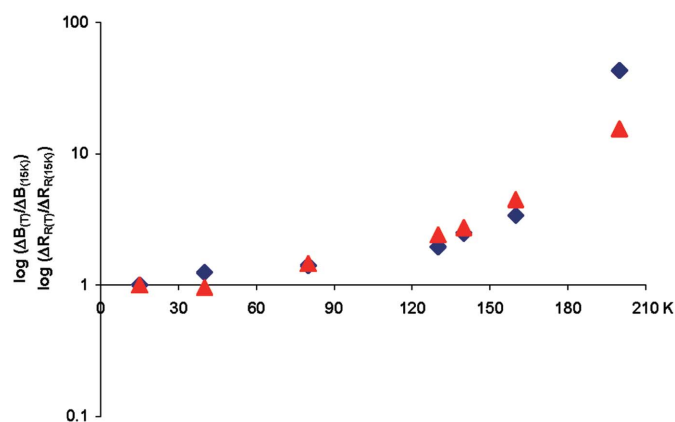
Figure 1
Temperature dependence of two components of radiation-induced changes in the structure factors, normalized to their values at 15 K. Diamonds show the rate of overall decay ΔB, and triangles show the rate of specific structure factor changes ΔR_R.

on the plot. Interestingly, the changes in the unit-cell parameters show a weaker dependence on temperature (Fig. 2, Table 3). It still remains to be determined to what extent the temperature dependence of radiation damage is affected by the chemistry of the solvent content and by crystal packing

Table 3
Global radiation damage indicators for GI-Ca data collected at different temperatures.

Units of the exposure time represent a 120 s exposure, ΔV_{ASU} is the change in the volume of the asymmetric unit cell during data collection, ΔB is the change in the overall B-factor expressed in Å^2, and R_R is the fractional change in magnitude of the structure factors. R_R values were calculated at resolution 4.0 Å.

	GI-Ca-15	GI-Ca-40	GI-Ca-80	GI-Ca-130	GI-Ca-140	GI-Ca-160	GI-Ca-200
Number of data sets used	6	8	4	4	4	4	2
ΔB	0.52	0.91	0.88	1.22	1.54	2.11	8.92
ΔB/(exposure time)	0.104	0.130	0.147	0.203	0.257	0.351	4.460
ΔV_{ASU}/(exposure time) (%)	+0.007	+0.014	+0.027	+0.018	+0.016	+0.016	−0.057
ΔV_{ASU}/ΔB (%)	+0.07	+0.108	+0.184	+0.089	+0.062	+0.046	−0.013
R_R (%)	1.1	1.5	1.9	3.2	3.6	5.9	6.8
R_R/(exposure time) (%)	0.22	0.21	0.32	0.53	0.60	0.98	3.40
R_R/ΔB	2.1	1.6	2.2	2.6	2.3	2.8	0.76

Table 4
The highest peaks calculated on radiation damage difference maps.

For each temperature, all data sets were used for the calculation of the radiation-damage difference maps (Table 1). The 15 peaks with the highest σ values are listed together with the overall number of peaks outside $\pm 4\sigma$. PDB file 2GLK (Katz *et al.*, 2006) was used as a source of model phases. Numbering of atoms, waters and/or solvent molecules is consistent with the numbering of PDB file 2GLK; the subscript indicates the type of atom in the cases where it was possible to identify it clearly, and NP indicates that the atom was not present in the original model.

|	Protein					
Peak height	GI-Ca-40	GI-Ca-80	GI-Ca-130	GI-Ca-140	GI-Ca-160	GI-Ca-200
1	H_2O 1048 (−16.6)	T_{OG1}119 (+16.4)	M_{SD}370 (−19.6)	M_{SD}370 (−13.6)	M_{SD}370 (−12.5)	M_{SD}370 (−9.1)
2	H_2O 1053 (−15.8)	H_2O 1048 (−15.8)	Mn 506 (−17.0)	E_{OE2}141 (−10.4)	Mn 506 (−12.4)	Mn 506 (+7.8)
3	H_2O 1097 (−14.2)	E_{OE2}141 (−15.0)	H_2O 1048 (−10.4)	H_2O NP (−10.4)	E_{OE2}141 (−9.5)	Mn 506 (+7.2)
4	E_{OE2}141 (−13.4)	H_2O 1097 (−13.6)	D_{OD1}101 (−13.5)	D_{OD1}101 (−10.2)	W_O137 (−8.6)	Mn 506 (−7.1)
5	Mn 505 (+13.2)	Mn 506 (−13.5)	H_2O 1117 (−12.3)	Mn 506 (−10.2)	H_2O NP (−8.6)	T_{OG1}90 (−6.8)
6	M_{SD}370 (−13.0)	T_{OG1}90 (−13.4)	W_O137 (−12.0)	W_O137 (−9.9)	Mn 505 (−8.3)	I_O59 (+6.6)
7	GOL_{O1}601 (−12.8)	T_{OG1}119 (−13.2)	H_2O 1097 (−12.0)	H_2O 1097 (−9.6)	H_2O 1048 (−8.3)	V_N72 (+6.2)
8	H_2O 1119 (−12.6)	M_{SD}370 (−12.7)	E_{OE2}141 (−11.6)	Mn 505 (−9.2)	H_2O 1097 (−8.3)	H_2O 1048 (−6.1)
9	T_{OG1}90 (−12.4)	H_2O 1053 (−12.5)	T_{OG1}90 (−11.1)	H_2O 1048 (−9.2)	W_{NE1}137 (−8.2)	I_O59 (−6.1)
10	H_2O 1053 (+12.2)	H_2O 1117 (−12.5)	Mn 505 (−11.0)	T_{OG1}90 (−8.9)	T_{OG1}91 (−8.1)	V_O98 (−6.1)
11	H_2O 1117 (−11.7)	D_{OD1}101 (−11.4)	M_{SD}380 (−11.0)	T_{OG1}91 (−8.5)	Mn 505 (−8.1)	H_2O 1048 (−6.1)
12	W_O137 (−11.2)	H_2O 1119 (−11.3)	H_2O 1053 (−10.6)	M_{SD}380 (−8.3)	H_2O 1119 (−8.1)	T_{OG1}17 (−6.0)
13	W_N137 (−10.9)	Mn 505 (+11.0)	H_2O 1078 (−10.5)	M_{SD}223 (+8.2)	T_{OG1}90 (−7.9)	E_O67 (−6.0)
14	Mn 506 (−10.4)	Mn 505 (−11.0)	T_{OG1}91 (−11.1)	H_2O NP (−8.2)	H_2O 1053 (−7.8)	H_2O 1239 (−5.9)
15	W_O137 (−10.3)	H_2O 1049 (−10.8)	H_2O 1119 (−10.3)	W_N137 (−8.1)	D_{OD1}101 (−7.6)	T_{OG2}82 (+5.8)
No. of peaks < −4σ or > 4σ	439	481	713	477	465	422
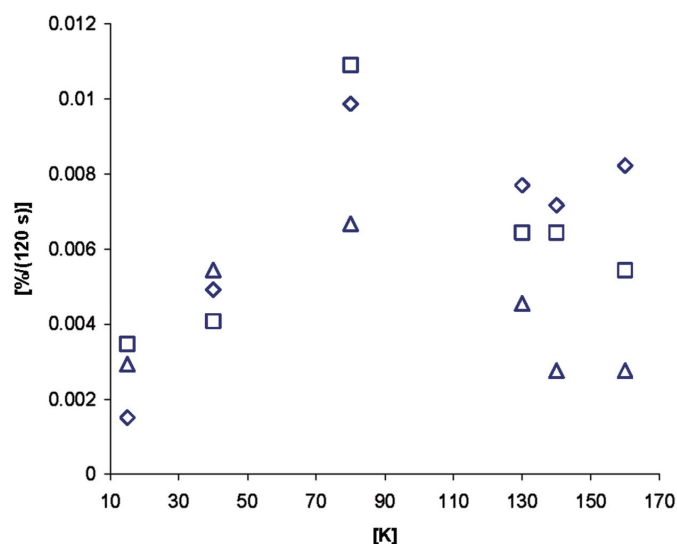
Figure 2
Temperature dependence of unit-cell dimension changes with radiation dose for glucose isomerase. The differences were calculated between the last and first data set (Table 1). Crystallographic unit-cell parameters are represented by *a* (triangles), *b* (squares) and *c* (diamonds).

(Weik, Kryger *et al.*, 2001; Weik, Ravelli *et al.*, 2001). The Fourier transforms of the initial changes of the structure factors indicate a similar spatial pattern of specific changes, which are, however, happening at different rates, as indicated by values of R_R/(exposure time) (Tables 3 and 4).

3.1.2. Unit-cell volume changes. For all the crystals, the unit cell changes gradually with the accumulated radiation dose, with crystal lattice repeats increasing slowly in most of the cases (Tables 3 and 5). For reasons that are not yet understood, there is a substantial variability in the rate of change in unit-cell parameters among different crystals of the same crystal form, which may be the source of the apparent peak at 80 K for the temperature series (Fig. 2). Such variability has been observed by others (Ravelli *et al.*, 2002; Murray & Garman, 2002). If there is a uniform expansion of the crystal lattice, the structure factors are essentially unaffected, while non-isomorphism does not require unit-cell changes. Thus, the unit-cell changes do not correlate well with other characteristics of radiation damage and, as has been previously recognized, they are not a good indicator of radiation damage impact.

Table 5
Global radiation damage indicators.

ΔV_{ASU} is the change in the volume of the asymmetric unit cell during data collection, ΔB is the change in the overall scaling B-factor expressed in $Å^2$, ΔM is the relative change in mosaicity of the crystal, R_R is the fractional change in magnitudes of the structure factors. The GI-Ca data collected at 40 K were used for comparison. For the 1G6X, 1NQF and NaI-841 data, ΔV_{ASU} was not calculated as either only one data set was available for each or different runs were collected with a different distance between the detector and the crystals. R_R values were calculated at 4.0 Å. ND = not determined.

	1G6X	1NQF	CAT	GI-Ca	GI-Mg	LT	LM	TH	NaI-841
ΔB	2.1	9.0	4.6	0.9	1.2	1.3	3.5	10.8	19.7
ΔV_{ASU} (%)	ND	ND	+0.66	+0.10	+0.11	+0.19	+0.56	+0.8	ND
$\Delta V_{ASU}/\Delta B$	ND	ND	+0.14	+0.11	+0.09	+0.17	+0.16	+0.07	ND
ΔM (%)	ND	+4.7	+53.5	+11.7	+6.8	+8.4	−6.0	−1.3	+3.6
$\Delta M/\Delta B$	ND	+0.52	+11.7	+13.0	+5.7	+6.3	−1.7	−0.12	+0.18
R_R (%)	2.2	9.6	6.2	1.5	2.9	2.5	2.5	7.7	5.1
$R_R/\Delta B$	1.0	1.1	1.4	1.6	2.4	1.9	0.7	0.7	0.26

3.1.3. Radiation-damage-induced changes at the atomic level. We observe large variability in the character of localized changes, from radiation damage concentrated in a single or a few positions to radiation-induced changes spread out widely across the protein volume.

The changes depend not only on the protein type, but also on the presence of active groups in the solvent. Comparison of monoclinic and tetragonal crystal forms of lysozyme shows that changes are localized in completely different places (Table 6, Fig. 3). Tetragonal lysozyme that crystallized from sodium acetate and sodium chloride has changes predominantly localized on disulphide bridges, whereas the monoclinic form that crystallized from sodium nitrate and sodium acetate has the largest changes present on nitrate groups with almost no peaks present on disulphide bridges. We interpret this observation as a nitrate group being preferentially targeted by electrons (Audette-Stuart *et al.*, 2005) over the disulphide

bridges. Thaumatin crystals show a pattern similar to tetragonal lysozyme, with radiation damage affecting most of the disulphide bridges at similar rates (Table 6) (Banumathi *et al.*, 2004). Bovine pancreatic trypsin inhibitor (BPTI) crystals show a different pattern, where one disulphide is damaged much faster than others, with sulfur of the cysteine in position 30 having by far the largest rate of electron density decrease (Table 6).

Other results refer to proteins that have no disulphide bridges. Glucose isomerase shows changes distributed over hundreds of sites. Nevertheless, the changes, even if numerous, are still concentrated in a relatively small fraction of the protein volume. The largest changes are listed in Tables 5 and 6. For the data (GI-Ca) collected at 0.9792 Å wavelength, above the Mn $K\alpha$ absorption edge (1.8961 Å), some of the largest changes are at the manganese positions, but not so at wavelengths below the Mn $K\alpha$ absorption edge
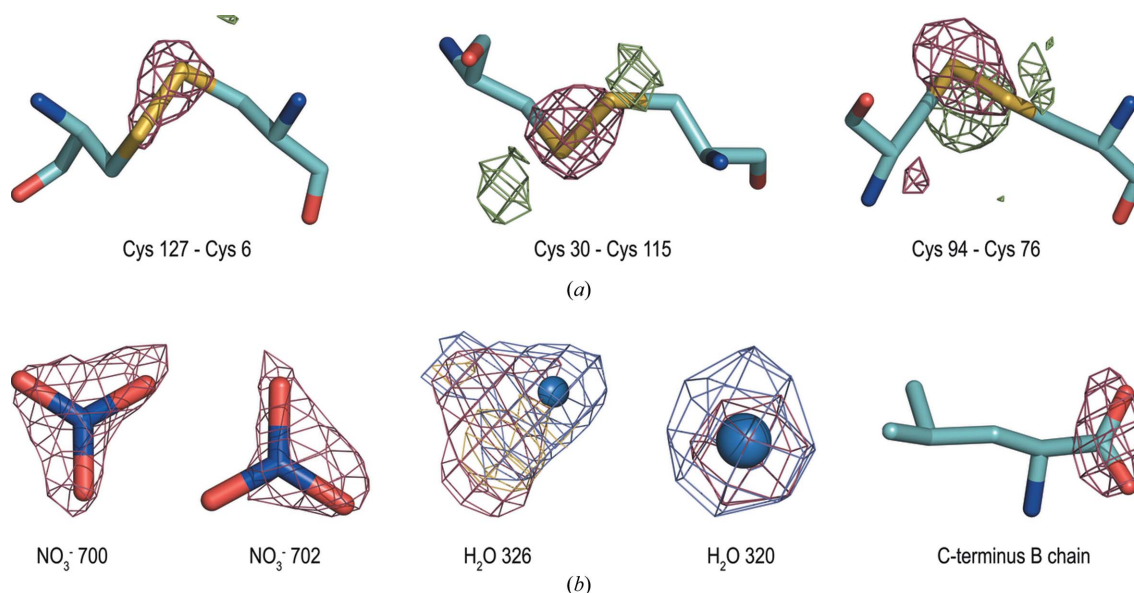
Figure 3
The most prominent radiation-induced specific changes in two crystal forms of lysozyme. Red: radiation damage map aF_o (where a is a slope coefficient obtained from the linear interpolation of radiation-induced changes of intensities, see §2.3) contoured at -4σ. Green: radiation damage map contoured at $+4\sigma$. Blue: $2F_o - F_c$ map contoured at 1σ. Orange: $F_o - F_c$ map contoured at $+3\sigma$. (*a*) Tetragonal lysozyme. The highest peaks are concentrated around three disulphide bridges; the positions clearly indicate that disulphide bridge Cys30–Cys115 is reduced. (*b*) Monoclinic lysozyme crystallized with sodium nitrate. The highest peaks are concentrated around nitrate ions, the changes around water 326 combined with the presence of positive $F_o - F_c$ map features and the $2F_o - F_c$ map indicates a nitrate ion rather than a water molecule. In the monoclinic form, both the C-termini are decarboxylated. There are no changes to disulphide bridges.

Table 6
The highest peaks on the radiation damage difference maps calculated from all the data for each crystal (Table 2).

Abbreviations used for the protein full names are defined in §2.1. For each protein the 15 peaks with the highest σ values are listed together with overall number of peaks outside of $\pm 4\sigma$. GI-Ca crystal collected at 40 K was chosen for comparison. Numbering of waters and/or solvent molecules is consistent with the numbering in the PDB deposits used for analyzing the specific changes. Superscripts indicate the protein chain for proteins containing more than one monomer in the asymmetric unit, and subscripts indicate type of atom in cases where it was possible to identify it clearly.

	Protein								
	1G6X	1NQF	CAT	GI-Mg	GI-Ca-40	LT	LM	TH	NaI-841
Model	1G6X	1NQF	4BLC	2GLK	2GLK	1IEE	1LJH	2BLR	1R61
1	$C_{SG}30$ (-43.3)	E465 $(+8.8)$	$E59^C$ (-8.9)	$D_{OD2}101$ (-9.4)	H_2O 1048 (-16.6)	$C_{SG}30$ (-12.8)	H_2O 326 (-8.2)†	$C_{SG}149$ (-7.9)	$T46^A$ $(+5.4)$
2	$C_{SG}51$ (-18.2)	E354 $(+8.5)$	$E70^C$ (-8.3)	$M_{SD}158$ (-9.0)	H_2O 1053 (-15.8)	$C_{SG}94$ (-12.0)	H_2O 326 (-8.0)†	$C_{SG}177$ (-7.8)	$I44^A$ (-5.2)
3	$C_{SG}14$ (-12.1)	D482 $(+8.0)$	$E70^B$ (-8.2)	$E_{OE2}141$ (-7.9)	H_2O 1097 (-14.2)	$C_{SG}94$ (11.3)	NO_3 702 (-7.9)	$C_{SG}193$ (-7.5)	R_C27^B $(+5.2)$
4	$C_{SG}14$ (-11.8)	E419 $(+8.0)$	$E70^A$ (-7.3)	$D_{OD2}101$ (-7.1)	$E_{OE2}141$ (-13.4)	$C_{SG}6$ (-8.3)	NO_3 700 (-7.2)	$C_{SG}126-$ $C_{SG}177$ (-7.4)	$T46^A$ $(+4.9)$
5	$C_{SG}38$ (-9.8)	D482 $(+7.5)$	H_2O (-7.2)	$E_{OE2}141$ $(+6.1)$	Mn 505 $(+13.2)$	$C_{SG}30$ $(+6.2)$	NO_3 700 (-7.1)	$C_{SG}71$ (-6.24)	$T_{OG1}48^B$ $(+4.9)$
6	C_N30 $(+8.6)$	E419 $(+7.5)$	$E190^D$ (-7.1)	H_2O 504 (-5.8)	$M_{SD}370$ (-13.0)	$C_{mc}94$ (-5.3)	$C-$terB (-6.7)	$C_{SG}146$ (-6.1)	$E_{OE2}124^A$ (-4.6)
7	$C_{CB}30$ (-8.6)	D316 $(+7.1)$	$E118^A$ (-7.1)	W_O137 (-5.8)	$GOL_{O1}601$ (-12.8)	$C_{SG}115$ $(+5.2)$	H_2O 320 (-6.7)	$D_{OD1}147$ (-5.4)	R_O86^B $(+4.4)$
8	C_O30 $(+8.4)$	D548 $(+6.6)$	$D127^D$ (-7.1)	$E_{OE1}221$ (-5.8)	H_2O 1119 (-12.6)	W123 $(+5.1)$	$C-$terA (-6.3)	$D_{OD}25$ (-5.4)	$K_{CG}187^B$ $(+4.4)$
9	$C_{CB}30$ $(+8.2)$	$S_{OG}374$ (-6.2)	$E190^D$ (-7.0)	$M_{SD}158$ $(+5.7)$	$T_{OG1}90$ (-12.4)	$D_{OD1}74$ (-4.8)	H_2O 365, H_2O 590 (-6.0)†	E4 (-5.2)	$M_{SD}181^B$ (-4.3)
10	C_O30 (-8.1)	$T_{OG1}467$ $(+6.0)$	$E59^B$ (-7.0)	$E_{OE2}373$ (-5.6)	H_2O 1053 $(+12.2)$	$C_{SG}76$ $(+4.5)$	$D_{OD1}87^B$ (-5.9)	$C_{SG}204$ (-5.2)	P_O153^A (-4.3)
11	$C_{SG}30$ $(+7.9)$	$MSE_{SE}317$ $(+5.9)$	$E118^C$ (-6.8)	$E_{COOH}141$ $(+5.6)$	H_2O 1117 (-11.7)	$C_{SG}115$ $(+4.5)$	$D_{OD1}119$ (-5.9)	$C_{SG}71-$ $C_{SG}77$ (-5.1)	$F_{CG}117^A$ $(+4.3)$
12	$C_{SG}30$ $(+7.8)$	$Q_{OE1}318$ $(+5.6)$	$D123^C$ (-6.8)	H_2O 676 $(+5.5)$	W_O137 (-11.2)	$C_{SG}6$ $(+4.5)$	$D_{OD1}87^B$ (-5.9)	$M_{SD}112$ (-5.1)	D_N79^B $(+4.1)$
13	$C_{SG}30$ $(+7.2)$	D44 $(+5.6)$	$E329^C$ (-6.7)	$M_{SD}370$ $(+5.4)$	W_N137 (-10.9)	$C_{SG}64$ $(+4.4)$	H_2O 253, H_2O 455, H_2O 532 (-5.7)†	$C_{SG}164$ (-4.9)	$H_{NE2}116^A$ $(+4.0)$
14	$C_{SG}30$ $(+7.1)$	$Q_{OE1}417$ (-5.6)	$D123^A$ (-6.7)	$M_{SD}379$ (-5.4)	Mn 506 (-10.4)	E7 (-4.3)	NO_3 700 (-5.7)	$C_{SG}71-$ $C_{SG}77$ (-4.7)	Solvent $(+4.0)$
15	$C_{SG}30$ $(+6.9)$	$S_{OG}374$ $(+5.4)$	$E59^A$ (-6.7)	$K_{NZ}289$ (-5.4)	W_O137 (-10.3)	D52 $(+4.2)$	H_2O 528, H_2O 265, H_2O 527 (-5.6)†	$C_{SG}134$ (-4.7)	R_O147^A (-4.0)
No. peaks $> -4\sigma$ or $< 4\sigma$	111	88	489	96	439	25	58	35	17

† Electron density maps indicate that these molecules are nitrate ions rather than water molecules. In PDB deposit 1LJH (Saraswathi *et al.*, 2002) used to analyze specific changes induced by radiation, the peaks were modelled as water molecules.

(GI-Mg, 2.0664 Å). However, the contribution of changes at the manganese positions to the overall structure factor changes induced by radiation is small. We have not found rotations and translations of the whole protein as being the source of significant structure factor changes in this case. We also analysed three cases of crystals with other heavy atoms, where the structure factor changes were limited (not much larger than experimental errors), even when heavily exposed. A NaI soak of APC35841 did not show the largest changes to be at the iodine positions (Table 6). In native bovine catalase the largest changes were decarboxylations (Table 6). There are additional electrons accumulating next to iron positions, suggesting that the iron is being reduced and has moved slightly. The changes observed at iron ion positions are rather small, but nevertheless should be considered when interpreting biochemical mechanisms. In the Se-Met derivative of 1NQF there is a surprising number of changes with positive electron density (Table 6). Rather than assuming that electrons accumulate there, we consider this as being a rather complex case, where a substantial part of the protein is damaged faster than other parts. In such a case, an overall B-factor scaling correction may result in a local contribution of $\mathbf{F}_c$ to the radiation damage map in areas that are less sensitive to radiation. This observation may indicate the need for even more complex models of radiation damage.
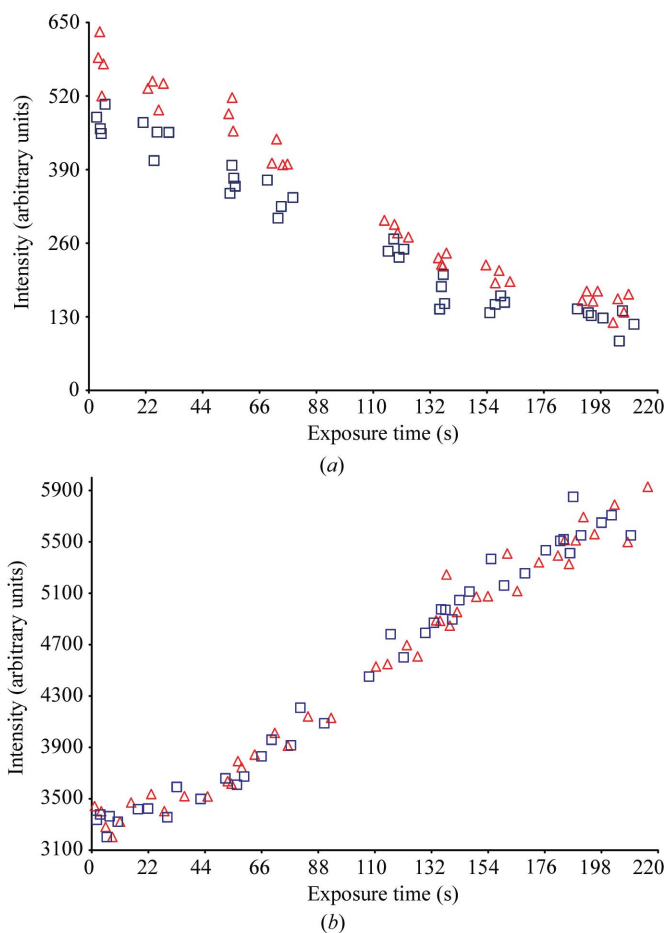
Figure 4
Change in diffraction intensity with exposure time for two reflections from GI-Mg. (a) The intensities of observations of the Friedel pair of the reflection with Miller indices (2 3 11) are shown. Triangles represent the intensities of reflection (2 3 11) and squares the intensities of reflection ($\bar{2}\bar{3}\bar{1}\bar{1}$). (b) As (a) but for the reflection with Miller index (2 5 3). The intensities were scaled together and corrected for overall decay so the changes in intensity presented here are due to specific structural changes.
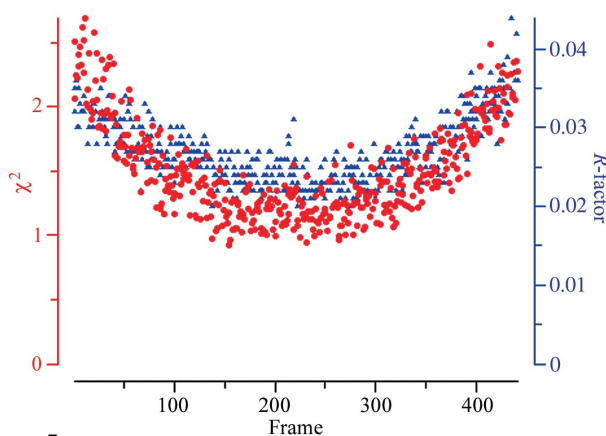
Figure 5
Statistics of scaling the individual images with the average of the data. The presence of radiation change creates a characteristic U-shape in the scaling statistics. Circles indicate $\chi^2 = \langle (I_n - \langle I \rangle)^2/\sigma_n^2 \rangle$ values for individual diffraction images, triangles show the traditional scaling R-factor $R = \Sigma_n |I_n - \langle I \rangle|/\Sigma_n \langle I \rangle$, where in both cases sums are evaluated for all measurements and where the centroid of the diffraction spot is in a particular image frame.

3.2. Data processing statistics in the presence of radiation-induced changes

As shown in Table 5, R_R could be very substantial in comparison with the expected phasing signals, even prior to the decay of the diffraction image. These radiation-induced changes, when not modelled in standard packages, produce large discrepancies between multiple measurements of observed intensities (Fig. 4). Such discrepancies affect all merging statistics and produce outliers outside the expected measurement error. The rejection of outliers assumes a sporadic error of potentially large magnitude, *e.g.* resulting from a superimposed reflection arising from an ice crystal. Radiation damage creates a very different pattern of disagreements that are of well defined magnitude and change uniformly with the increased radiation dose. The rejection of such outliers effectively removes the observations made at the beginning and/or the end of data collection. It is not clear whether eliminating such observations helps to estimate phasing signals. Not applying automatic rejection may even be superior, because the average intensity of individual reflections over the whole data collection is close to the intensity corresponding to the middle dose. Without removing the outliers, the average dose in each of the Friedel pair will be similar, so the calculated anomalous difference will be affected much less than by the overall change in intensities resulting from radiation. The fact that reflections in the middle of the overall exposure time are closer to average than reflections at the beginning and the end creates a characteristic U-shaped plot of χ^2 as a function of exposure time (Fig. 5) (Ramagopal *et al.*, 2005). The χ^2 discrepancy statistics are a function of both the speed of the structure factor changes and the precision of the measurements. With high redundancy, a moderate size U-shape is of little consequence, even without correcting for radiation-caused structural alterations. It is definitely not worthwhile in such a case to increase the expected errors; it is better to leave the average χ^2 statistics higher than 1.0, as the radiation damage affects the Friedel mates about equally (Fig. 4). However, when the radiation-induced changes are large, modelling structure factors as a function of the accumulated dose gives a substantial improvement in phasing. This was confirmed by solving all the test cases presented here with the SAD method. In the case of catalase, only the iron atom substructure was determined. In all other cases, the structures were solved even when the Bijvoet differences were extremely weak.

4. Conclusions

The intense beam radiation damage is one of the main factors that have to be considered in experiment planning. What is always present is the scaling B-factor increase, to a good approximation behaving as a linear function of the dose (Kmetko *et al.*, 2006). This creates a fundamental limit in how long we can collect useful data, since the resolution will decrease with the dose. Correcting for overall decay of diffraction intensity in the scaling procedure does not elim-

inate other changes, where the structure factors go up and down with the dose. These changes of individual reflections are uniform with the dose, and in most experiments can be approximated by a linear function within the data errors. Analysis of the Fourier map calculated from the slopes of this linear interpolation identified different structural patterns of change in different proteins and even in different crystal forms of the same protein.

Radiation effects strongly influence the diffraction experiments at high-flux beamlines. The lifetime of the crystal is limited either by decay or, in some cases, by a macroscopic fragmentation of the crystal lattice (Murray *et al.*, 2005). The latter shows a rapid increase in mosaicity, up to the point when integration fails. Prior to such integration failure, the merging statistics suddenly deteriorate without other explanation. The only thing that can be done if this happens is eliminate such bad data from the set. Even within a set of images where the deterioration is small, the radiation-induced changes can be substantial. However, the molecular-replacement method is not sensitive to them, up to the point of interpreting the structure. In some cases the active-site structure can be sensitive to radiation, *e.g.* in the case of redox groups or chromophores (Yano *et al.*, 2005; Baxter *et al.*, 2004).

The simplest approach to reducing radiation damage is to use a low level of exposure with large crystals to provide a sufficient scattering power. Unfortunately such crystals are often not available and increasing the dose to obtain enough photons in the Bragg peaks makes radiation-induced changes likely to be larger than the phasing signal. A historical solution, still valid, is to use heavy-atom isomorphous differences, which are very large. An effective approach to eliminating the influence of radiation-induced changes is to measure dispersive differences at the same time. An elegant method, unfortunately not practical in many cases, is to collect data with the twofold axis of the crystal aligned with the oscillation axis, which is precisely perpendicular to the beam. Alternatively one can apply a so-called inverse-beam method, where segments of data related by a 180° rotation are collected close in time. This method requires a very precise goniostat, and may not be possible when a very fast data collection is desired. With larger crystals a practical method is to follow a simple protocol, *e.g.* continuous oscillation, with a very large redundancy. This approach has allowed structures with extremely weak anomalous signals to be solved (Ramagopal *et al.*, 2003). The increase in scaling *B*-factor is the best indicator of the crystal decay, and the U-shaped plot of χ^2 as a function of time is the first sign of radiation changes having an impact on data quality. To optimize the experiment one should be aware of radiation-damage characteristics of the particular crystal form studied. To transfer experience from past data collections, we propose a simple method to quickly calibrate the experimental station. Small, about 100 µm in size, crystals of tetragonal lysozyme can be grown quickly, even at a synchrotron site, by following a modified recipe communicated by Stura [§2.1 (Stura, 1998)]. The presence of iodine anions increases the absorption of X-rays in crystals and, consequently, the radiation damage, so the substantial increase in *B*-factor can be quickly accomplished. The small size of the crystals makes them fully illuminated by the beam and avoids the excessive saturation of the detector. The high symmetry of lysozyme results in reliable scaling and determination of the increase in *B*-factor even with a small amount of total oscillation, as little as 10°. Such a lysozyme crystal provides a very good reference for other data and can potentially identify problems with cryo-cooling.

There are still many questions about radiation damage and possibilities for improvement. The addition of radical scavengers should be further investigated for their potential in reducing radiation damage. Cooling to very low temperature with helium is currently cumbersome and comes with a cost, but its value for enhancing data quality should encourage the building of experimental-friendly systems. Modelling of radiation-induced changes (Diederichs, 2006; Diederichs *et al.*, 2003), and even their use in phasing, has already started (Schiltz *et al.*, 2004; Ravelli *et al.*, 2003), but is in an early phase and much more can be expected in the future.

We are witnessing the continuous development of experimental crystallography methods. Gains from each component (helium temperature cryo-cooling, correcting for radiation-induced changes, using massive redundancy) are multiplicative, so all of them need to be pursued. We can expect that the future will allow us to collect more structural information, particularly from crystals that intrinsically scatter weakly, now a frequent occurrence in crystallographic studies of the biologically most interesting cases.

References

Addlagatta, A., Krzywda, S., Czapinska, H., Otlewski, J. & Jaskolski, M. (2001). *Acta Cryst.* D**57**, 649–663.
Audette-Stuart, M., Houee-Levin, C. & Potier, M. (2005). *Radiat. Phys. Chem.* **72**, 301–306.
Banumathi, S., Zwart, P. H., Ramagopal, U. A., Dauter, M. & Dauter, Z. (2004). *Acta Cryst.* D**60**, 1085–1093.
Baxter, R. H. G., Seagle, B. L., Ponomarenko, N. & Norris, J. R. (2004). *J. Am. Chem. Soc.* **126**, 16728–16729.
Burmeister, W. P. (2000). *Acta Cryst.* D**56**, 328–341.
Chimento, D. P., Mohanty, A. K., Kadner, R. J. & Wiener, M. C. (2003). *Nature Struct. Biol.* **10**, 394–401.

Diederichs, K. (2006). *Acta Cryst.* D**62**, 96–101.

Diederichs, K., McSweeney, S. & Ravelli, R. B. G. (2003). *Acta Cryst.* D**59**, 903–909.

Katz, A. K., Li, X. M., Carrell, H. L., Hanson, B. L., Langan, P., Coates, L., Schoenborn, B. P., Glusker, J. P. & Bunick, G. J. (2006). *Proc. Natl. Acad. Sci. USA*, **103**, 8342–8347.

Kmetko, J., Husseini, N. S., Naides, M., Kalinin, Y. & Thorne, R. E. (2006). *Acta Cryst.* D**62**, 1030–1038.

Murray, J. & Garman, E. (2002). *J. Synchrotron Rad.* **9**, 347–354.

Murray, J. W., Rudino-Pinera, E., Owen, R. L., Grininger, M., Ravelli, R. B. G. & Garman, E. F. (2005). *J. Synchrotron Rad.* **12**, 268–275.

Nave, C. (1995). *Radiat. Phys. Chem.* **45**, 483–490.

Nave, C. & Hill, M. A. (2005). *J. Synchrotron Rad.* **12**, 299–303.

O'Neill, P., Stevens, D. L. & Garman, E. F. (2002). *J. Synchrotron Rad.* **9**, 329–332.

Otwinowski, Z. & Minor, W. (1997). *Methods Enzymol.* **276**, 307–326.

Otwinowski, Z. & Minor, W. (2000). *Denzo and Scalepack. International Tables for Crystallography*, Vol. F, edited by M. G. Rossmann, p. 226; 235. Dordrecht: Kluwer.

Otwinowski, Z. *et al.* (2007). In preparation.

Owen, R. L., Rudino-Pinera, E. & Garman, E. F. (2006). *Proc. Natl. Acad. Sci. USA*, **103**, 4912–4917.

Ramagopal, U. A., Dauter, M. & Dauter, Z. (2003). *Biophys. J.* **84**, 355A–356A.

Ramagopal, U. A., Dauter, Z., Thirumuruhan, R., Fedorov, E. & Almo, S. C. (2005). *Acta Cryst.* D**61**, 1289–1298.

Ravelli, R. B. G., Leiros, H. K. S., Pan, B. C., Caffrey, M. & McSweeney, S. (2003). *Structure*, **11**, 217–224.

Ravelli, R. B. G. & McSweeney, S. M. (2000). *Structure*, **8**, 315–328.

Ravelli, R. B. G., Theveneau, P., McSweeney, S. & Caffrey, M. (2002). *J. Synchrotron Rad.* **9**, 355–360.

Saraswathi, N. T., Sankaranarayanan, R. & Vijayan, M. (2002). *Acta Cryst.* D**58**, 1162–1167.

Schiltz, M., Dumas, P., Ennifar, E., Flensburg, C., Paciorek, W., Vonrhein, C. & Bricogne, G. (2004). *Acta Cryst.* D**60**, 1024–1031.

Stura, E. A. (1998). *Strategy 3: Reverse Screening, Crystallization of Proteins: Techniques, Strategies and Tips. A Laboratory Manual*, edited by T. M. Bergfors, pp. 113–124. International University Line.

Teng, T. Y. & Moffat, K. (2000). *J. Synchrotron Rad.* **7**, 313–317.

Weik, M., Berges, J., Raves, M. L., Gros, P., McSweeney, S., Silman, I., Sussman, J. L., Houee-Levin, C. & Ravelli, R. B. G. (2002). *J. Synchrotron Rad.* **9**, 342–346.

Weik, M., Kryger, G., Schreurs, A. M. M., Bouma, B., Silman, I., Sussman, J. L., Gros, P. & Kroon, J. (2001). *Acta Cryst.* D**57**, 566–573.

Weik, M., Ravelli, R. B. G., Kryger, G., McSweeney, S., Raves, M. L., Harel, M., Gros, P., Silman, I., Kroon, J. & Sussman, J. L. (2000). *Proc. Natl. Acad. Sci. USA*, **97**, 623–628.

Weik, M., Ravelli, R. B. G., Silman, I., Sussman, J. L., Gros, P. & Kroon, J. (2001). *Protein Sci.* **10**, 1953–1961.

Yano, J., Kern, J., Irrgang, K. D., Latimer, M. J., Bergmann, U., Glatzel, P., Pushkar, Y., Biesiadka, J., Loll, B., Sauer, K., Messinger, J., Zouni, A. & Yachandra, V. K. (2005). *Proc. Natl. Acad. Sci. USA*, **102**, 12047–12052.